



HAL
open science

Direct numerical simulation of a subcritical coaxial injection in fiber regime using sharp interface reconstruction

Jean-Christophe Hoarau, Luc-Henry Dorey, Davide Zuzio, Florian Granger,
Jean-Luc Estivalezes

► To cite this version:

Jean-Christophe Hoarau, Luc-Henry Dorey, Davide Zuzio, Florian Granger, Jean-Luc Estivalezes. Direct numerical simulation of a subcritical coaxial injection in fiber regime using sharp interface reconstruction. 2023. hal-04212765v1

HAL Id: hal-04212765

<https://hal.science/hal-04212765v1>

Preprint submitted on 20 Sep 2023 (v1), last revised 2 Sep 2024 (v3)

HAL is a multi-disciplinary open access archive for the deposit and dissemination of scientific research documents, whether they are published or not. The documents may come from teaching and research institutions in France or abroad, or from public or private research centers.

L'archive ouverte pluridisciplinaire **HAL**, est destinée au dépôt et à la diffusion de documents scientifiques de niveau recherche, publiés ou non, émanant des établissements d'enseignement et de recherche français ou étrangers, des laboratoires publics ou privés.

Direct numerical simulation of a subcritical coaxial injection in fiber regime using sharp interface reconstruction.

J.-C. Hoarau^a, L.-H. Dorey^a, D. Zuzio^b, F. Granger^a, J.-L. Estivalezes^b

^aDMPE, ONERA, Université Paris-Saclay, F-91123 Palaiseau - France

^bONERA / DMPE, Université de Toulouse, F-31055 Toulouse - France

Abstract

The numerical simulation of space launchers combustion chambers is a topic of increasing interest, as it may help the development of safer and more efficient designs. Understanding fuel injection is a particularly severe challenge. The liquid oxygen is injected by a round orifice surrounded by an annular gaseous stream of fuel, leading in sub-critical conditions to a two-phase assisted atomization process. The result of this process is a very dense and polydisperse two-phase flow, which strongly influences the behaviour of the chamber. Experimental investigation of this flow is difficult due to the axisymmetric geometry and the dense characteristic of the spray. Neither RANS nor Large Eddy Simulation (LES) do possess reliable models able to reproduce the smallest scales of atomization, one of the reasons being the lack of relevant experimental data. The objective of this work is therefore to provide detailed information on the atomization process using Direct Numerical Simulation. This paper presents a DNS simulation of a coaxial liquid-gas assisted atomization in the typical fiber-regime encountered in cryogenic injectors. The objective of this study is to better understand the liquid topology evolution, and to extract relevant information which may help the development of larger scale models. The simulation realised on more than 80 000 cores, allowed the resolution of structures as small as 1/80 of the jet diameter. The flow was analysed at first in terms of topology statistical data, using a dedicated detection and classification algorithm able to characterise the individual liquid structures. These include the main liquid dart, the ligament created during primary atomization and the spherical droplet obtained at the end of the atomization process. Subsequently, a more global statistical topology indicator was investigated, namely the interface density distribution. This quantity is nowadays used in larger scale RANS or LES models to predict the smallest scales of atomization, and it is therefore of the utmost importance to understand its behaviour on a realistic case. The interface density distribution was correlated to the global jet behaviour and the liquid topology data obtained by the detection algorithm. The results showed, in particular, a strong correlation between the initial increase of liquid-gas interface density with the generation of ligaments and between the continuous decrease of the interface density during droplets formation and stabilization.

Keywords: Primary atomization, coaxial injector, liquid rocket engine, DNS, textural atomization

1. Introduction

Liquid rocket engines rely on high-energy assisted atomization to produce the best oxidant-fuel mixture for optimal combustion. When sufficiently low temperature and pressure conditions are encountered in the chamber, the oxygen is injected as a liquid phase, while the fuel is injected in the gaseous form. These conditions are called "sub-critical" and are typically encountered during engine's ignition, for specific permanent regimes of the low thrust engines, and during low thrust phases of more powerful throttleable engines. The injection system consists of a round liquid oxygen jet,

surrounded by an annular, high-speed gaseous fuel (hydrogen or methane) flow. The interaction between these flows triggers two-phase instabilities, which lead to liquid breakup, and subsequent atomization.

Two main stages can be distinguished in the assisted atomization process [1]. The first occurs near the orifice, here, the liquid becomes subject to longitudinal instabilities ([2], [3], [4], [5]), which are the results of the shearing effect triggered by the interaction between the liquid and gas flows. The instabilities involved in this phase are the Kelvin-Helmholtz, induced by the interfacial shearing, and the Rayleigh-Taylor, induced by the heavy liquid acceleration [5]. Both sheared liq-

Nomenclature

$\bar{(\bullet)}$	Temporal average	ρ_l	Liquid density
$\langle \bullet \rangle_\theta$	Azimuthal average	σ	Surface tension
J	Momentum Ratio	Σ	Liquid-gas interface density
Re_g	Gas Reynolds number	VOF	Volume of fluid
We_g	Gas Weber number	ϕ	Level-set
Re_l	Liquid Reynolds number	δ_g	Vorticity length
We_l	Liquid Weber number	d_{30}	Liquid structure characteristic diameter
U_g	Gas injection Velocity	δ_{lip}	Lip length
U_l	Liquid injection Velocity	D_l	Liquid injector diameter
ρ_g	Gas density	h_g	Gas injection gap

uid round jets at low Weber numbers and sheets main bodies present a similar flapping motion in this zone, as reported by [6], [7] and [8]. This zone usually extends up to several diameters from the nozzle, where the main breakup point is reached. The liquid forms at this point a population of individual structures, in particular elongated stream-wise ligaments. All these phenomena make up primary atomization. The secondary atomization occurs when the released liquid structures are in turn affected by the shearing gas flow, in a continuous fragmentation in smaller and smaller structures up to the final spray under the Rayleigh-Plateau instability ([9], [10], [11]). Coaxial jet atomization regimes can be classified in function of the aerodynamic Weber number. [12] described five regimes: axisymmetric Rayleigh breakup, non-axisymmetric Rayleigh breakup, membrane breakup, fiber breakup, and super-pulsating breakup, in function of the gaseous Weber number and the liquid Reynolds number. In [13] the momentum flux ratio M was added as a relevant non dimensional number to the Weber and Reynolds numbers. More recently, four breakup regimes were distinguished by [14]: first-wind induced breakup regime ($We_a \approx 9$), second-wind induced breakup regime ($We_A \approx 50$), bag breakup regime ($We_A \approx 150$) and the fiber-type atomization ($We_a \approx 500$). This last regime is common in liquid rocket engines. In this regime, the liquid core stretches under the gaseous stresses, and periodically releases large liquid blobs in the stream. The instabilities growing on the liquid core develop in many stream-wise thin ligaments, which subsequently undergo Rayleigh-Plateau breakup. This mechanism generates a complex

two phase flow within a few jet diameters from the injection point, in which the liquid core coexists with large liquid structures, ligaments and the first droplets.

The assisted atomization is believed to play a significant role in the global behaviour of the chamber. In particular it may participate, together with the thermal and acoustic behaviour of the thrust chamber, to the development of combustion instabilities. The prediction and control of combustion instabilities is still a very challenging task, as several complex mechanisms may interact. The experimental approach is a meaningful way to better study the instability onset and development. However, full-scale engine tests are very expensive, and the measurement systems face severe restrictions in the operating conditions of a combustion chamber. Atomization poses the particular challenge of a dense liquid-gas zone investigation: even with available optical access, the liquid topology is unavailable near the injector. Peripheral droplets populations can be detected and measured, but there is little information about their formation mechanisms.

Direct Numerical Simulation (DNS) can provide useful information about primary atomization. Appropriate numerical methods have been developed in the last decades to simulate the complex two-phase flows of atomization. The Level-Set approach and its variant, the Conservative Level-Set (CLS), were employed at first to simulate low density ratio diesel jets and liquid jet in cross-flow (LJICF) ([15] and [16]). The Volume-of-Fluid (VOF) approach was used to simulate the breakup of a liquid jet by a high-speed coaxial gas-jet ([17], [18]). The two approaches were coupled by [19] in the

Coupled Level-Set/Volume of Fluid method, and used to simulate turbulent jet atomization ([20], [21], [22]). CLS and CLSVOF were used to simulate the primary atomization of a gas sheared liquid sheet by [23] and [24], albeit with reduced density ratios. In [25], [26] and [27] DNS simulations of air-assisted thick film atomization were performed. The results were analysed in terms of interfacial waves development, turbulence and two-phase mixing layer development, two-phase flow turbulence.

Numerical simulation of a coaxial air-water jet was performed in [28] using a CLSVOF approach, making use of a modified extrapolated liquid velocity field to ensure proper liquid kinetic energy preservation and a LES approach for both liquid and gas flow. The considered ambient pressure air-water configuration was taken from [29]. The OpenFOAM VOF approach was used in [30] to perform simulations of the primary breakup of high-viscosity glycerol-water-mixture using an external mixing twin fluid nozzle. Compressible large eddy simulations (LES) were performed to capture the morphology of the primary breakup as well as the important flow field characteristics. The VOF approach was used to track the unsteady evolution and breakup of the liquid jet. This work reported good agreement with respect to breakup frequency, velocity fields and morphology of the liquid jet. The low Weber regime was however unfavourable for atomization, and the liquid jet showed mostly large scale deformations only induced by pulsating and flapping instabilities. In [31], an extensive study of primary atomization behaviour of high-viscous liquid (glycerol-water mixture) jets was performed again with the OpenFOAM VOF approach. Different gas pressures were investigated. The simulations showed a pulsating mode instability of liquid jet, along with a fiber-type disintegration. This study focused on the very dense zone of primary atomization in terms of liquid core length and kinetic energy distribution. However, the analysis did not extend to the atomised liquid. Moreover, in that case, the viscosity ratio μ_l/μ_g is very high around 5500, giving liquid Reynolds number of the order of 35, far from the case that interests us. It should be noticed that all these LES approaches for atomization simulations did not take into account subgrid scale modelling of surface tension force. Indeed, as they work with a one-fluid approach for interfacial flow, this LES modelling must be understood as dealing only with the velocity field. Besides interface capturing methods described above, other so-called multi-fluid approaches are often used to simulate multiphase flows in a context of compressible flows, contrary to the previous ones mainly used for incompressible flows. These approaches can

be classified in the family of diffuse interface methods, since the interface is no longer captured or tracked, but rather represented by the volume fraction of each phase in each computational cell which is transported by the local velocity field. It should be noted that although this method, for the same mesh size, is less accurate than an interface capturing method, it is easily generalized to the case of unstructured meshes. Indeed, this method was successfully employed by [32, 33] to catch the primary atomization of an airblast atomizer at room conditions in the framework of large-scale LES-like simulations. In order to simulate, in an industrial context, the two-phase flow from the injection system to the combustion of the final spray, it is not realistic to envisage direct simulations. On the other hand, a multi-fluid approach for the primary atomization coupled with a dispersed phase approach for the secondary atomization seems to be a good candidate. Using this strategy, full multi-scale LES simulations of a sub-critical cryogenic LOX-GH2 fiber-regime jet were performed in [34] and [35] by explicitly coupling a multi-fluid diffuse interface method (for the dense zone or primary atomization zone) with an Eulerian dispersed phase solver (for the remaining dispersed zone). However in the transition zone between dense and dispersed ones, the size and velocity of droplets were estimated as a function of the injected propellant properties and imposed as a boundary condition and not deduced from the dense zone. One way to overcome this shortcoming is to use an elsa-type model initially developed in a RANS context [36] and [37], to apply it here in an LES context. As in turbulence RANS modelling, an additional quantity is followed in time, namely the liquid-gas interface surface area per unit of volume. This quantity can statistically represent the dispersion of the liquid in the local volume of control. The general form of the corresponding equation is a transport-diffusion, with multiple source terms representing production by turbulent mixing between liquid and gas, mean shear stress, break-up, and destruction by coalescence or evaporation. Despite the several propositions of source terms closure in RANS ([38], [39], [40]) and LES formalism ([41], [42], [43]), it remains difficult to understand the actual behaviour of this quantity: the validation is often realised by comparing the final outcome of atomization, i.e. the final droplet size, with experiments. Indeed, in particular for the coaxial jet configuration, the experimental investigation are strongly limited by the density of the produced cloud of liquid structures, mainly along the jet centerline: superposition of the liquid structures hampers in this region the visual detection techniques, so that the only available data involves the more dilute small droplets population

on the jet periphery.

2. Numerical tools

2.1. Physical model

ONERA has been developing its in-house two-phase flow Direct Numerical Simulation solver, called DYJEAT, since 2004 [44]. DYJEAT was successfully employed to simulate complex two-phase flows. [45] simulated low to high speed droplet impacting a either dry or wet solid wall. DYJEAT reproduced the assisted atomization of a liquid sheet ([24, 46]) and a high density ratio liquid jet in cross-flow ([47]). DYJEAT model involves the direct numerical resolution of the incompressible Navier-Stokes equations. A one-fluid sharp interface method is used to simulated two non-miscible phases. The interface is tracked in space and time in order to define the local properties of the fluid by a Level-Set function, coupled to a Volume-of-Fluid approach to ensure mass conservation. The liquid and gas properties will be respectively referred to with the subscripts l and g . The two-phase incompressible Navier-Stokes equations read:

$$\frac{\partial \phi}{\partial t} + U \nabla(\phi) = 0 \quad (1)$$

$$\frac{\partial C}{\partial t} + \nabla \cdot (UC) = -C \nabla \cdot U \quad (2)$$

$$\nabla \cdot U = 0 \quad (3)$$

$$\frac{\partial \rho U}{\partial t} + \nabla \cdot (\rho U \otimes U) = f + \nabla \cdot T \quad (4)$$

Where U is the velocity vector, ρ the density and f the external body forces such as gravity. ϕ is the Level-Set function, C the liquid volume fraction in each cell. The stress tensor is modeled as follows:

$$T = -pI + D \quad (5)$$

$$D = \mu (\nabla U + (\nabla U)^T) \quad (6)$$

Here p represents the hydrodynamic pressure, μ the dynamic viscosity and D the viscous stress tensor. Jump conditions across the interface are set as follows. The normal velocity is conserved across the interface $U_l \cdot n = U_g \cdot n$. Viscous and pressure effects are balanced by the surface tension effect and velocity no slip condition, :

$$[p] - n \cdot [2\nabla U] \cdot n = \sigma \kappa \quad (7)$$

$$t \cdot [2\nabla U] \cdot n = 0 \quad (8)$$

Where σ is the surface tension, κ the local curvature, t and n the tangential and normal unit vectors oriented

from gas to liquid. The symbolic $[\cdot]$ represents the jump across the interface, $(\cdot)_l - (\cdot)_g$.

2.2. Numerical model

Level-Set and Volume-of-Fluid are widely spread in literature for two-phase flow simulations. The Level-Set function allows for accurate computation of interface properties at the expense of mass conservation issues, whereas the VOF method ensures mass conservation. For these reasons, the Coupled Level Set-Vof method has been developed by [19] and [20]. This approach uses both Level-Set and VOF functions to track the liquid, providing an accurate and reliable method to simulate two-phase flows. The Level-Set function, ϕ , represents the signed distance between any points in the domain and the interface. It is a scalar field driven by the scalar transport equation (1).

The interface location is provided by the zero level curve of ϕ . Interface properties are calculated by :

$$n = \frac{\nabla \phi}{\|\nabla \phi\|} \quad (9)$$

$$\kappa = \nabla \cdot \left(\frac{\nabla \phi}{\|\nabla \phi\|} \right) \quad (10)$$

The Level-Set loses its properties of distance function during its advection. That loss is minimized by the redistance algorithm [48] which updates the Level-Set field's till the $\|\nabla \phi\| = 1$ is discretely satisfied while keeping the zero level curve untouched. A reinitialization step is performed at each timestep.

The color function C in the VOF method is defined for an incompressible flow as the volume fraction of liquid in each cell as:

$$C(x_i) = \frac{V_{li}}{V_i} \quad (11)$$

$$V_i = V_{li} + V_{gi} \quad (12)$$

with i the cell index and V_i its volume. The color function is a scalar field driven by a conservation equation reading:

$$\frac{\partial C}{\partial t} + \nabla \cdot (CU) = 0 \quad (13)$$

The interface is approximated in each cell by a plane, the so-called PLIC reconstruction from [49]. The normal vector components are inferred from the surrounding Level-Set values whereas the plane itself is shifted to ensure that the bounded volume corresponds to the VOF value. The VOF PLIC allows for geometrical flux

computation [19], requiring a directional splitting algorithm. Once the VOF is advected, the Level-Set function is locally shifted to be consistent with the local VOF value, thus ensuring mass conservation. The freeware VofTools library from [50] has been used to deal with the geometrical computations involving the interface reconstruction.

Momentum conservation considerations led the authors to develop the corresponding energy preserving algorithm, called Conservative Momentum scheme, in [47]. The CMOM approach involves the use of the PLIC fluxes to compute momentum fluxes and solve a conservative form of the momentum equation. Using the mass fluxes (ρU) in both mass and momentum equation ensures consistency between mass and momentum, and global preservation of each phase energy. The resulting scheme dramatically improves the solver robustness and accuracy when dealing with high flows at density ratio and large phase velocity differences. The Ghost-Fluid method [51] allows for subgrid accurate computation of the pressure and stress tensor jumps. The continuous solution is extended on the two sides of the interface, and a corresponding source term is added in the numerical discretization.

2.3. Liquid structures detection

As presented in the introduction, the massive dispersion of various multi-scale liquid objects in atomization processes makes the study of their distribution a very complex subject. In order to obtain statistics on the distribution, shape and size of the liquid structures generated in a spray a new detection algorithm was developed in the DYJEAT platform [52]. This new tool, called AlgoDetect, can detect, classify and characterise individual liquid structures into a parallel computing environment. The detection and characterisation is performed at runtime, so that it is not necessary to store a huge amount of time solutions, and the temporal resolution can be arbitrarily chosen in function of the timestep.

The detection provides information about each liquid structure, such as the centre of mass position, its extent in each direction, its surface area, or its volume. The output is consequently light in terms of storage. This tool allows the code to analyse full 3D fields without any significant impact on the runtime or the storage needs: without this innovative tool, many of the analyses presented below would have been prohibitively expensive or simply impossible.

The CPU cost of detection depends strongly on the number of droplets and their spatial distribution, but in this case, the detection time is between 8 and 10 times

the iteration time. Detection is then only performed every 250 iterations in order to limit the computing resources added to the simulation. Observations of the detection revealed that more frequent detection of structures is not necessary as visual tracking of drops is already possible at this frequency.

The algorithm is built to perform structure detection and classification. This means that, once the raw data have been collected, the liquid shape is analysed and the structure is tagged in one of the following categories:

- **Droplet:** this category contains all the structures which can be considered as spherical droplets, which are unlikely to undergo further breakup unless submitted to extreme shearing;
- **Ligament:** these particular structures are the typical elongated structures generated in many assisted atomization regimes, in particular the fiber regime which is the focus of the current work. Ligaments are highly unstable structures as they rapidly undergo Rayleigh-Plateau instability and transform in several child droplets;
- **Liquid core:** this is the main body, attached to the liquid injection hole.
- **Liquid Structure:** in this work, liquid structure is a generic term referring to any of the detected isolated liquid structures, including Droplets and Ligaments, minus the Liquid Core.

3. Simulated configuration

This paragraph details the physical and numerical configurations for the simulation presented later in this paper. A schematic representation of the coaxial injector geometry modelled for the simulation is shown in Figure 1. This configuration was chosen to reproduce the case simulated by Rutard [53] in his thesis. The case is a reproduction of an experimental case used in the CORIA laboratory [54, 55].

The computational domain consist in a rectangular box of sizes $[L_x \times L_y \times L_z] \simeq [18.6 \times 5.8 \times 5.8] \times D_l$. With L_y and L_z the width and depth of the simulation and L_x the simulated domain's length plus the injector's length. The injector is modelled using immersed interface method [56] and the mesh refinement is analysed in detail in the following section. In addition, the resolution is also sufficient to correctly represent the lip of the injector, with several points in the lip length δ_{lip} . The mesh size is imposed to $dx = 0.17 \delta_{lip}$

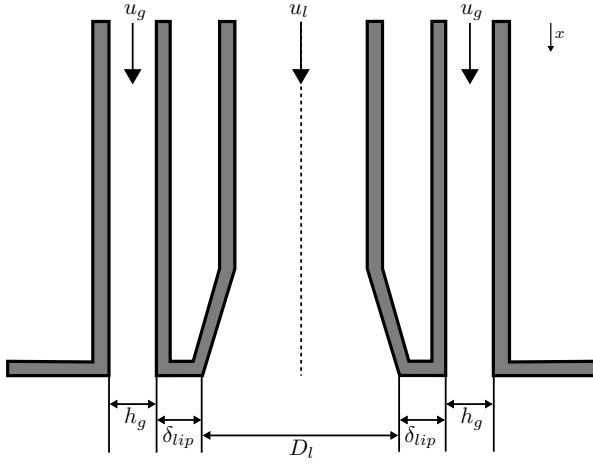


Figure 1: Scheme of the injector geometry

The fluids are injected in the lower x face of the cube by a Dirichlet inflow condition on the velocity, VOF, and ϕ fields. The liquid is introduced in the central part of the injector and the gas in its outer ring around the liquid jet with a high velocity compared to the liquid. Non-turbulent uniform velocity profiles are imposed in the boundary condition, although the simulation domain includes a small portion of the injector of length $L_{inj} \approx 1.8 D_l$. The injector help establish realistic injection conditions in the gas and liquid. On all the walls of the back-plate of the injector, a no-slip boundary condition is imposed, and on all other faces outflow boundary conditions are considered. Finally, the time step is imposed so that the CFL number does not exceed 0.5 in all the domains. This condition provides a time step around 1.8×10^{-7} s after the transient regime.

It is important to notice that for numerical reasons, the pressure is imposed at 10 bar to reduce the density ratio between the two phases. Consequently, the gas density has been multiplied by 10 compared to Rutard [57]. Therefore, other physical parameters (gas velocity, gas dynamic viscosity, and surface tension) of the typical air/water configuration of [57] have been tweaked to conserve the characteristic adimensionalized values: Reynolds number *ie.* $Re_l \approx 10^4$ and Weber number *ie.* $We_g = 490$ calculated with the liquid velocity and liquid diameter. The resulting momentum ratio is $J \approx 4$. The operating point is still in the fiber regime by referring to the qualitative graph of regime repatriations given by [13].

4. Mesh and temporal convergence analysis

4.1. Mesh refinement study

The spatial resolution required to perform a direct numerical simulation is a crucial point in the setup of a massive simulation like the present DNS. In single-phase flow, it is well established that the Kolmogorov micro-scale evaluates the universality of turbulence diffusion scales, so that mesh convergence can be considered as achieved once the mesh size is able to capture this scale. However, in multi-phase flow, this topic is still an open question. The unknown is in this case the size of the smallest physical droplet created during the atomization process. On the other hand, it can be argued that it would probably not be necessary to capture these smallest scales if the associated liquid mass is a negligible fraction of the total liquid mass.

In the present work, a preliminary assessment of the encountered droplet sizes was made. This estimation was performed using an empirical correlation available in the literature, namely, the average ligament "size" $\langle D_0 \rangle$ given by Marmottant *et al.* [5] :

$$\langle D_0 \rangle \approx 0.23 \lambda_T, \quad (14)$$

with:

$$\lambda_T = 2.8 \delta_g We_{\delta_g}^{-1/3} \left(\frac{\rho_l}{\rho_g} \right)^{1/3}, \quad (15)$$

$$\delta_g = 5.6 h_g Re_g^{-1/2}, \quad (16)$$

where the Reynolds and Weber numbers defined from the gas are defined by:

$$Re_g = \frac{\rho_g h_g u_g}{\mu_g}, \quad (17)$$

$$\text{and } We_{\delta_g} = \frac{\rho_g u_g^2 \delta_g}{\sigma}. \quad (18)$$

Using the physical characteristic chosen for the present simulation, the resulting non-dimensional numbers would be $Re_g \approx 10^4$ and $We_{\delta_g} = 7.8$, resulting in a size of the atomised ligaments around $\langle D_0 \rangle \approx 0.55 \delta_{lip}$. Exploiting the available computing resources, a regular Cartesian grid composed of 2.8 billion points distributed as $[N_x \times N_y \times N_z] = [3072 \times 960 \times 960]$ allowed a spatial resolution of $dx = 0.17 \delta_{lip}$. Considering this result, the mesh size of $dx = 0.17 \delta_{lip}$ would be sufficient to impose 3 points in the main structures of the primary atomization process.

On the other hand, it is difficult to assess the actual number of grid points needed to resolve a given liquid structure. In consequence, a mesh de-refinement

study was carried out, in order to compare the characteristics of the scales resolved with each mesh level. Two more simulations were performed using reduced cell sizes. Besides the main simulation using a cell size of $dx_{fine} = 0.17 \delta_{lip}$, a second one employed a cell size of $dx_{middle} = 0.255 \delta_{lip}$, while a third one employed a cell size of $dx_{coarse} = 0.34 \delta_{lip}$. To quantitatively compare the performances of the three meshes, the global distribution density functions (*pdf*) of the diameter $d_{30} = \sqrt[3]{V_d}$, where V_d is the droplet volume, were extracted from the three simulations. The probability density functions were built using a Gaussian kernel estimation with the following function :

$$pdf_{h_s}(x) = \frac{1}{nh_s} \sum_{i=1}^n K\left(\frac{x - x_i}{h_s}\right), \quad (19)$$

where n is the number of droplet considered, h_s the smoothing parameter and K the Gaussian kernel function. In the estimation, the smoothing parameter of each density is imposed at $h_s = 0.0075 \delta_{lip}$ resulting in a good trade-off between the smoothing and the resolution of the *pdf* of the three cases considered. The results are plotted in Figure 2.

The difficulty in comparing *pdf* estimated with different mesh resolutions is the inherent normalisation of *pdf* that keeps their integral equal to 1. Figure 2 a) compares the *pdfs* from the three mesh configurations using directly the equation (19). The shapes of the distributions are similar, with a peak value near $2 dx_{current}$ where $dx_{current}$ is the cell size of the relative case. However, the absolute values of the *pdfs* are different: this difference is due to the number of droplets changing drastically between cases. Therefore, considering that a coarse and a fine mesh should simulate the same structures as long as they are resolved on both mesh, Figure 2 b) now compares the *pdfs* normalised by the ratio of the drops number of the finer mesh n_{fine} over the number of drops of the current mesh n .

This last comparison shows clearly that once normalised, the middle and coarse cases distributions fit very well up to the resolution limit of $2 dx_{current}$. Hence, we can conclude that the middle and coarse case can well reproduce the droplets diameter distribution up to this value. Transposing this conclusion to the fine case means that the proposed DNS simulation can correctly describe the droplet diameter distribution up to the peak of the distribution corresponding to $2 dx_{fine}$ *i.e.* $0.34 \delta_{lip}$. This conclusion is coherent with the typical Nyquist criterion reasoning that says it must be at least three points *i.e.* two cells in each direction to resolve a droplet correctly.

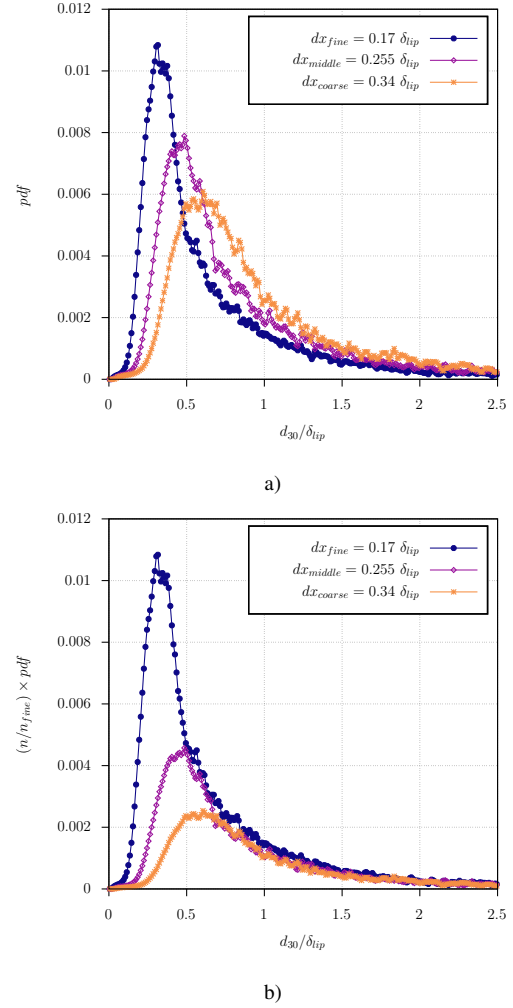


Figure 2: Comparison of probability density function with different mesh resolution. a) *pdf* estimation using the formula (19), b) *pdf* with a scaling factor (n/n_{fine}) .

To comfort this argumentation, the *pdf* in Figure 3 were made using only the resolution threshold of the coarser grid. It is important to notice that no scaling were performed on those *pdf*, only a selection of the considered structures. Using this selection method, the three *pdfs* superpose again very well. To conclude the convergence study, an estimation of the spatial accuracy of the atomization simulation could be obtained, with a spatial "confidence" threshold on the simulated droplet size. The analysis proposed in the paper will be therefore performed on the "physical" structures larger than the threshold, while the smaller ones will be discarded as numerical artefacts.

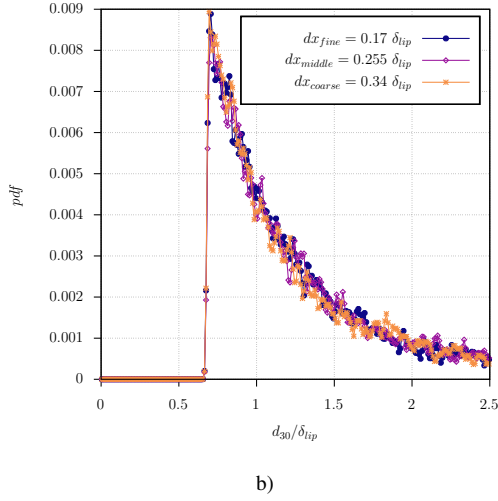


Figure 3: Comparison of probability density function with different mesh resolution considering in each case only droplets bigger than the resolution threshold of the coarser grid.

4.2. Convergence of time-averaged quantities

The present configuration is highly unsteady. Therefore, the record of time-averaged value is necessary to extract valuable results of this DNS in order to calibrate models used in future LES calculations. Due to the tremendous amount of computational resources necessary in this simulation, the transient regime of the flow is simulated without recording the means variables to save storage and CPU resources. Consequently, some careful effort has been made to estimate the beginning of the established regime. However, in a complex dynamic flow like assisted atomization, evaluating some flow-through time or transient-time is not an easy task. The most straightforward idea is to calculate the transient-time using a characteristic speed in the flow. However, fluid velocities change rapidly in the flow, yet neither the gas nor the liquid injection velocities are good candidates for a characteristic velocity. The gas is indeed rapidly slowed down by the shear with the liquid, and the acceleration of the liquid by the gas strongly depends on the droplet diameter formed in the flow. The velocity proposed in equation (20) is used to take the differences in fluid momentum into account, in which J is the momentum ratio of the gas and liquid.

$$V_w = \frac{U_g + JU_l}{1 + J}, \quad (20)$$

Using this definition the characteristic velocity is equal to $V_w = 5.78 \text{ m/s}$, the corresponding flow-through time can be evaluated as $\tau_w = L_x/V_w = 0.018 \text{ s}$. In unsteady simulations, the common idea is to perform sev-

eral flow-through times to evacuate the transient region. Once again, due to the high computational resources needed in this simulation, only two flow-through times are considered to evacuate the transient regime. That brings the end of the transient at $t = 0.036 \text{ s}$.

Besides this qualitative evaluation, other quantities have been monitored to confirm the evacuation of the early transient part of the simulation. The first quantity is the evolution of the continuous liquid core presented in Figure 4. At $t = 2\tau_w$, represented by the solid vertical line in the figure, the liquid core has already shot two large structures as the rapid drops around $t = 0.024 \text{ s}$ or $t = 0.032 \text{ s}$ indicates. After that, the liquid core oscillates around its mean value and seems roughly established. The second quantity, presented in Figure 5, is the evolution of the number of small droplets *ie.* with a characteristic length $\sqrt[3]{L_x L_y L_z} \in [0, 5dx]$ (where L_x, L_y, L_z are respectively the length of the structures in the direction x, y and z). The estimated transient time is also represented in this figure with the vertical solid line. This second quantity is interesting because it greatly represent the main goal of this work that is simulating the atomization process. Furthermore, this quantity is a good indicator of the global flow establishment because small droplets are distributed over all the domain, as shown in figure 6. At $t = 2\tau_w$, the stabilization of the number of small droplets per iteration also confirms the evacuation of the transient regime.

Consequently, the temporal mean values have been recorded from $t = 2\tau_w = 0.036 \text{ s}$ until this end of the calculation *ie.* between $t = 0.036 \text{ s}$ and $t = 0.073 \text{ s}$. The averaging time is below the necessary time to achieve a perfect convergence of the means values, although the calculation will be continued in future works. The recorded temporal averaging quantities are the three velocity components, VOF , Σ , and the fluctuations of those variables.

5. Analysis of the liquid flow topology

5.1. Global description of the flow solution

The configuration of an assisted atomization jet in the fiber regime exhibits a complex dynamic with multi-scale structures. A global visualisation of the simulated flow is proposed in Figure 6 in which the iso-contour $\phi = 0$ is displayed in yellow, representing the liquid interface. In addition, the transverse plane $z = 0$ is colored in grey-scale with the velocity magnitude to materialise the gas injection in the chamber. The dark-grey left-most plan is the iso-contour $\phi_{sol} = 0$ representing the solid surface of the injector. In the center of this plan,

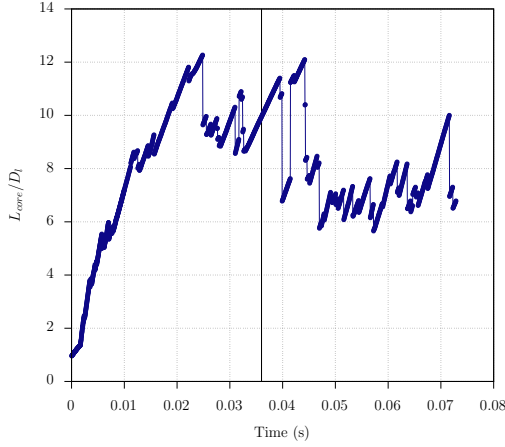


Figure 4: Continuous liquid core evolution and the estimated transient time (solid vertical line).

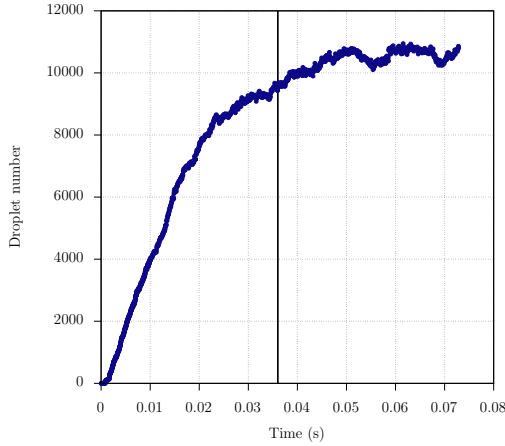


Figure 5: Evolution of the total number of droplet with $\sqrt[3]{L_x L_y L_z} \in [0, 5dx]$ and the estimated transient time (solid vertical line).

the beginning of the gas injector is noticeable, and the liquid interface covers the liquid part of the injector.

The flow structure is very complex, with many intricate multi-size structures spread all over the domain. The first feature to be described is the liquid core, number 1 in Figure 6. In this zone the liquid core shows the development of the streamwise instabilities, which deform the interface. The second one is the location of the primary atomization, with the development of many ligaments of different shapes and sizes. The third one presents a polydispersion of large liquid detached ligaments and droplets, which assume a spherical shape under the effect of surface tension. These three zone are investigated in detail in the following sections. The analysis will be based on the results of the detection and classification algorithm, which allows a quantitative de-

scription of the local flow in terms of topology. Figure 7 shows a classification result on a snapshot of the liquid field. The liquid core, in yellow, extends from the injector to about one-third of the domain, with an increasingly complex shape due to the formation of ligaments. The detached ligament, in red, are found in consequences from the periphery of the main jet, and travel downstream under the convective flow. Droplets are mainly generated from the breakup of the ligaments, and become predominant far from the injector.

5.2. Destabilization of the liquid core

The spray caused by the atomization takes its origin in the liquid core oscillations generated by the fast surrounding gas jet. This section analyses some essential features of the liquid core to understand the genesis of the atomization process in zone 1. In Figure 6, longitudinal instabilities appear as soon as the liquid jet leaves the injector. In the close instantaneous view in Figure 8 a) lots of early destabilization waves are visible on the liquid core generated by the rapid gas flow. Those waves seem to be caused by the vortex shedding building up in the gas downstream the injector outlet. In this area, two different structure types are noticeable. The first ones are small ripples on the surface only visible in the vicinity of the injection, identified on Figure 8 b) by red circles. The second ones seem more energetic but they are hard to observe in 3D visualisations of the liquid core. Those structures are only visible on slices of the interface, as in Figure 8 b), identified by blue circles.

In order to further characterise the structures just described, a frequency analysis of the interface displacement is developed in the following. For three different locations away from the back plate, the position of the liquid core interface is recorded in the four cardinal directions. The four directions are denoted in the following as Y^+ Y^- Z^+ and Z^- and the three positions correspond to $x/D_l = 0.5$, $x/D_l = 1$ and $x/D_l = 1.5$. At each x location, Fourier transform analysis is performed on each recorded signal and the four spectra are averaged to bring out the principal structure frequencies. These averaged spectra are plotted at the three x locations in the figure 9.

This frequency analysis clearly shows a significant amplification of structures between 302 and 357 Hz. This spike frequency matches the energetic structures identified by the blue circles in Figure 8 b). Besides this large spike, around 350 Hz, smaller peaks are visible between 500 and 700 Hz. These could correspond to the smaller structures identified using the red circles in Figure 8 b).

Time: 0.064389

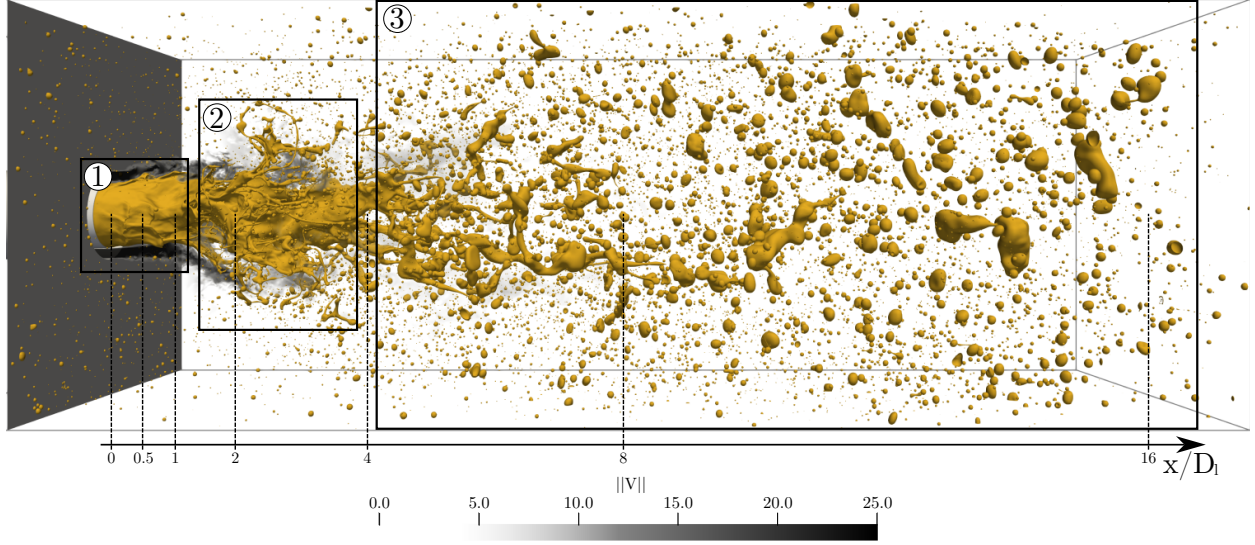


Figure 6: Global visualization of an iso-contour of the interface in yellow together with a slice of velocity magnitude in black and white in the middle plane of the domain. Three zones can be distinguished in the flow : 1) the destabilization zone, 2) the atomization zone, 3) the stabilization zone.

The origin of those specific frequencies is not clear and their genesis of the instabilities could be assessed using the frequency content of sensors in well chosen locations in the gas. Unfortunately, during the main simulation *ie.* $dx_{fine} = 0.17 \delta_{lip}$, the recording of high frequency sensors was not yet implemented. In the middle resolution case however, the velocities have been recorded in some locations. This information give some clues in understanding the behaviour of the gas flow and the origin of the frequency found on the interface displacement. At three x locations, the streamwise velocity has been recorded at a frequency of around 165 kHz by 8 sensors shared around a circle whose radius is equal to $(D_l + h_g)/2 + \delta_{lip}$ the middle of the injector gas channel. Averaged spectra given in Figure 10 are obtained at $x = 0.5 D_l$ and $x = 1 D_l$ from these sensors. They confirm the building up of specific frequencies in the gas and the major amplification is observed for 309 Hz . This frequency perfectly corresponds to the large structures previously described in the interface displacement. The spectra also depict smaller amplification of frequencies between 350 Hz and 890 Hz . These structures are also consistent with the small ripples described in the previous paragraphs. Those two observations indicate that the disturbances seen on the interface come from the turbulence and vortex shedding of the gas injection.

5.3. Droplet creation mechanism

To properly study the droplet creation mechanism, the central location of the atomization must be correctly located. As can be observed visually in the Figure 6, zone 2 seems to have the highest droplet concentration. In order to provide quantitative data and refine the location of this area, some spatial statistics have been performed using the individual droplets information provided by the AlgoDetect tool. As analyzed in section 4.1, the droplets are correctly resolved if they have an equivalent diameter $d_{30} > 2 dx$. The following analyses therefore exclude drops smaller than this resolution criterion.

As the individual droplets detected by the algorithm are identified by their center of mass, the numerical domain was discretized in a large number of macro-cells, each macro-cell spanning several mesh cells in each direction. The macro-cells constitute therefore a regular Cartesian grid, each macro-cell having a $800\mu m$ size. The valid liquid droplets are then regrouped into the macro-cells according to the position of their center (clustering). Finally, to take in account the three dimensional distribution of the droplets, the clustered distributions have been averaged in the azimuthal direction (in a similar way than Figure 15). In the following, all quantities that have been averaged azimuthally will be noted with $\langle \bullet \rangle_\theta$. Those statistics used all 420 snapshots of the ϕ equally spaced in time from 0.0331 s

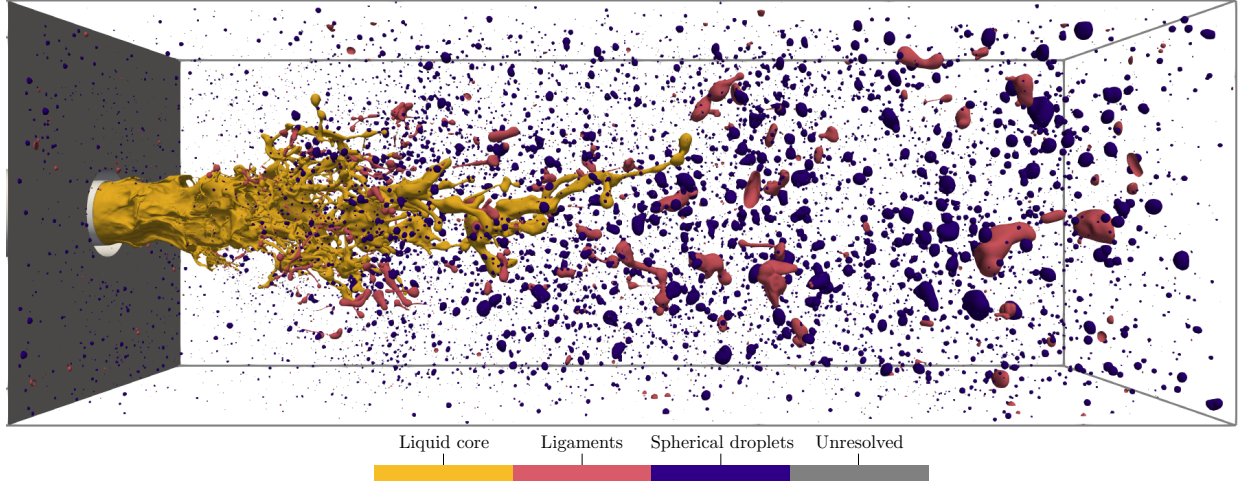


Figure 7: Visualisation of the core, the ligaments and spherical droplets detected in a snapshot of the flow.

to 0.0728 s in the simulation. The acquisition time $t_{acc} = 0.0728 - 0.0331 = 0.0397\text{ s}$ is used in all the following to adimensionalized the different analyses.

The first and more straightforward analysis done using this procedure is counting all the valid droplets, i.e. which are not excluded by the resolution criterion. The resulting distribution is presented in Figure 11, superposed to the same zone 2 boundaries as in Figure 6. Drops stuck on the back plate are not taken into account in the count because their behaviour is not of interest here. The distribution shows maximum values located in the middle of zone 2, confirming the location of the dominant atomization process in this zone. An interesting remark can be made on the distribution by qualitatively comparing the present results with Le Touze *et al.* [35]. The model used in [35] predicts a strong formation of fine drops very close to the injection, on the contrary here zone 1 shows a large area in which almost no drops are observed. is necessary for the formation of the first drops. However, this comparison should be taken with caution as there are significant differences between the conditions considered in [35] and the present simulation.

The surface instabilities which develop on the liquid core generate large pockets of liquid. With the action of the fast flow of gas, these large pockets expand to their point of rupture, where they become elongated structures called ligaments. The ligaments rapidly undergo Rayleigh-Plateau breakup, splitting themselves in many droplets. At the end of the breakup, the liquid

has reached a stable state where all the resulting structures are spherical droplets, which do not undergo further atomization unless they are submitted to a renewed high shearing effect. A visual example of a break-up chronology of a ligament just detached from a pocket is presented in Figure 13. Figure 13 a) presents a long ligament just detached from the core. Then, in the following Figures 13 b) and c), the structures generated by this ligament are tracked. These three figures illustrate the typical break-up mechanism and stabilization into spherical droplets occurring in the fiber regime. Figure 12 depicts similarly the average characteristic liquid structure size distribution

The calculation of the average diameter over a cluster is therefore weighted using the volume of each structure to counteract this bias. The average characteristic diameter D_v is then defined as follows:

$$D_v = \frac{\sum d_{30,p} V_p}{\sum V_p}, \quad (21)$$

where the sums consider each structure of a cluster, V_p is the volume of a structure, and $d_{30,p} = \sqrt[3]{V_p}$ is a characteristic diameter often used in the literature to study atomization. . These plots confirm the characteristics of the flow depicted in figure 7: a large number of smaller droplets are visible near the primary atomization zone, while a population of larger droplets, coming from the stabilization of the larger axial ligaments, characterize the second half

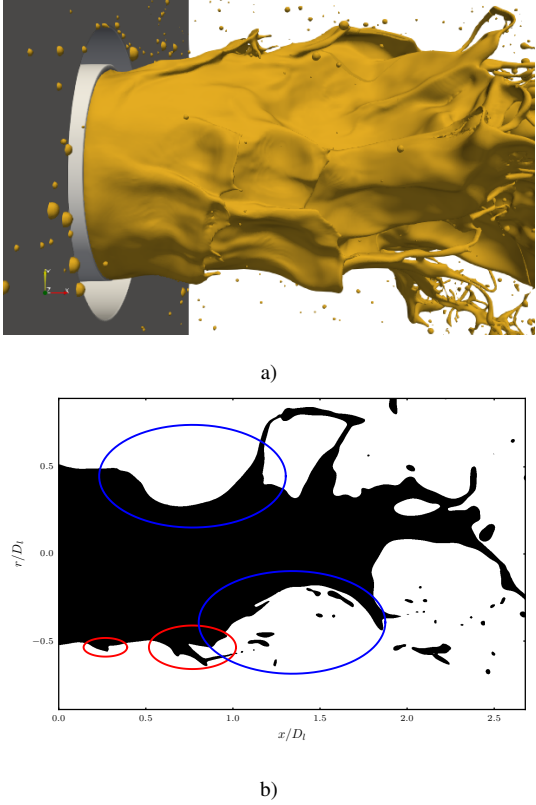


Figure 8: a) Focus on the destabilization wave on the liquid core. b) Instantaneous slice ($z = 0$) with the liquid phase in black. The red circles locate the tiny ripples, and the blue ones are the energetic structures strongly destabilising the core.

5.4. Ligament characteristics

The process of atomization depicted in Figure 13 is directly due to the shear stress of the gas. It is well described in Dumouchel *et al.* [58] and defined as textural atomization. The creation of droplets seems to first spend most of the time through the formation of detached ligaments, so their detection is a good indicator of the progress of this textural atomization. Therefore, detached ligament identification is made in post-processing using the data available after the AlgoDetect procedure. Two geometrical criteria are defined by equations (22) and (23) to detect ligaments structures:

$$\frac{\text{Max}(L_x, L_y, L_z)}{\text{Min}(L_x, L_y, L_z)} > C_1, \quad (22)$$

$$\text{and} \quad \frac{V}{\frac{\pi}{6} L_x L_y L_z} < C_2, \quad (23)$$

where L_x , L_y , and L_z are the dimensions of the rectangular box containing the liquid structure, V its volume,

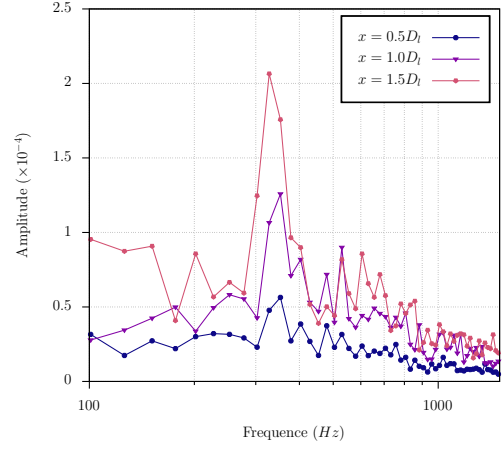


Figure 9: Frequency analysis of the interface displacement at three axial positions.

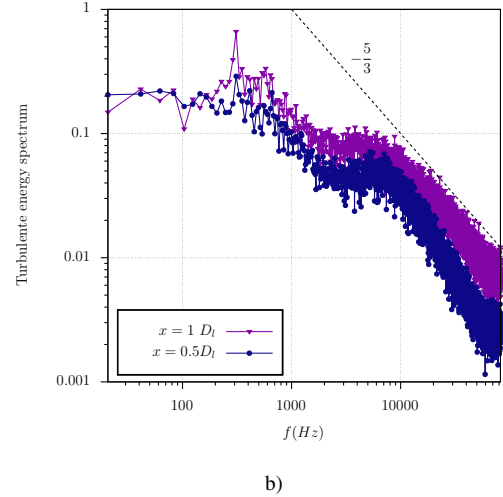


Figure 10: Frequency analysis of turbulent energy on the middle case i.e. $dx_{middle} = 51 \mu\text{m}$.

and C_1 and C_2 constants wisely chosen to select the desired structures. In the following, those constants have been imposed at $C_1 = 1.6$ and $C_2 = 0.5$. The first criterion defined in equation (22) measures the aspect ratio of the bounding box of the structures. It therefore accurately detects elongated structures in the direction of the mesh, as shown in Figure 14 a). However, this criterion does not detect ligaments when they are diagonal to the mesh, as in Figure 14 b), because their bounding box is almost cubic. In this case, it is mandatory to have another criterion in order to detect these ligaments. The second criterion defined in equation (23) compares the volume of the structure with the volume of an ellipsoid contained in the same box as the structure. These cri-

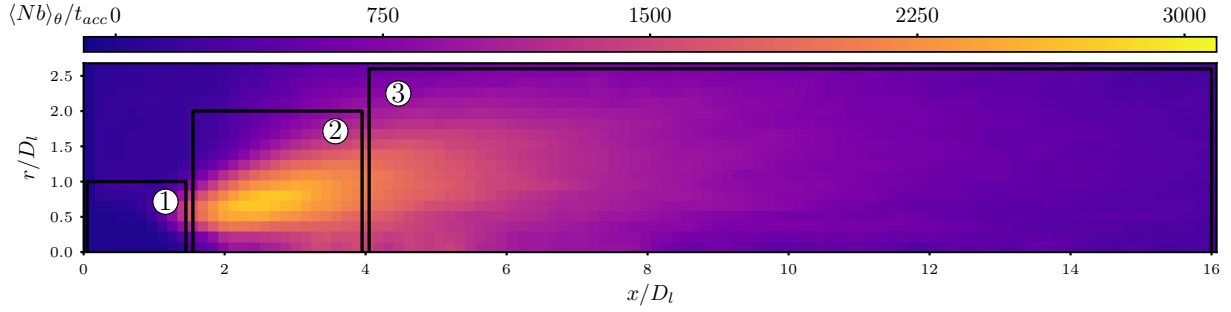


Figure 11: Distribution of droplet count gathered in all snapshots recorded in the DNS dimensionalized by acquisition time.

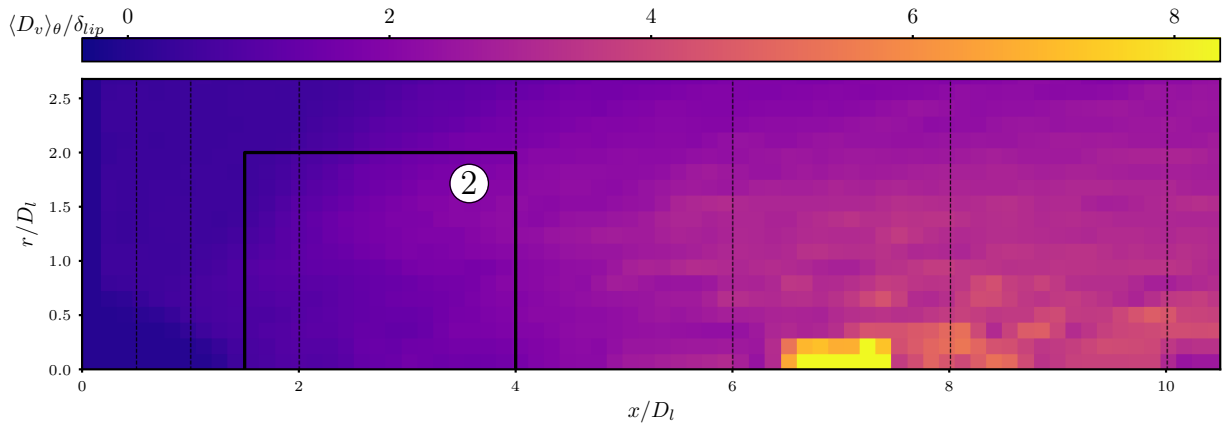


Figure 12: Averaged structure size distribution recorded in all the snapshots of the simulation.

teria are therefore complementary and allow the detection of most ligament structures as shown in Figure 7. Spherical droplets are remaining resolved liquid structures that are not detected by the criterion (22) and (23). Unresolved structures are liquid structures with a size under the resolution limit characterized in section 4.1.

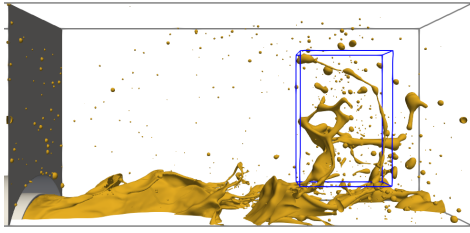
Those criteria allow the detection of most ligaments, however, it is hard to predict the behaviour of ligaments because of their various shapes and sizes. The early stage of atomization generates many very small ligaments. These structures quickly transform into numerous very small droplets. Downstream, ligament structures are still present but they are significantly larger. Those larger ligaments seem to come from two different sources. The first ones, as early small ligaments, come from pockets of textural atomization [58] occurring later in the flow where the gas no longer has enough energy to strongly disrupt them. The second ones are structures coming directly from the center of the liquid core named structural atomization in [58]. Those two last types have a much longer stabilization time and do

not produce many child structures or spherical droplets.

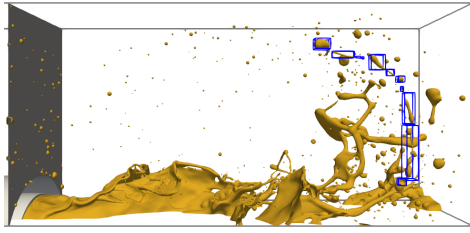
All those observations demonstrate the central role of the ligaments in the atomization process. The direction, velocity, and sizes of the final droplets seem to derive directly from the characteristics of ligaments. Moreover, their large ratio of surface over volume could strongly impact the averaged surface density. The relation between ligaments and surface density must be clarified because many authors directly use the surface density to model atomization without considering the presence of ligaments in the process. Therefore, Figure 7 perfectly highlights their possible small dimensions, and in some LES frameworks, those ligaments could easily be unresolved.

6. Interfacial surface study

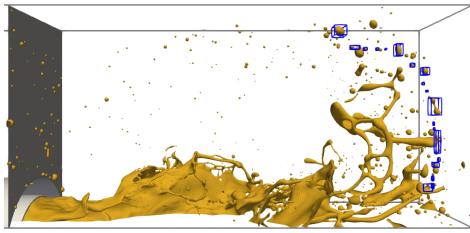
The following analysis focuses on the interface surface. In the interface density models, this quantity is used to statistically describe the dispersion of the local liquid mass, its topology being unknown. Using the re-



a)



b)



c)

Figure 13: Tracking of structures coming from a ligament just detached from a liquid pocket in three subsequent snapshots.

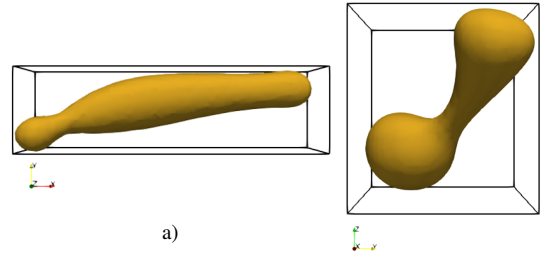
solved DNS fields, the spatial distribution of the computed surface can be extracted and correlated to the local physical phenomena occurring during primary atomization. Appropriate models can therefore be developed upon this knowledge.

6.1. Average surface density behaviour

The interfacial area density is computed in each cell by the ratio between the surface and the volume of the liquid :

$$\Sigma = \frac{S_{\text{PLIC}}}{V_{\text{cell}}}, \quad (24)$$

with S_{PLIC} the area of the interface plane from the PLIC reconstruction (see section 2.2) and V_{cell} the volume of the cell. The (24) quantity was computed in all the simulation domain for all the available time-steps, and these fields were averaged in time and in space, in the azimuthal or streamwise direction to obtain the axial pro-



a)

b)

Figure 14: Examples of ligaments in different configurations a) aligned in the direction of the mesh b) diagonal to the mesh directions.

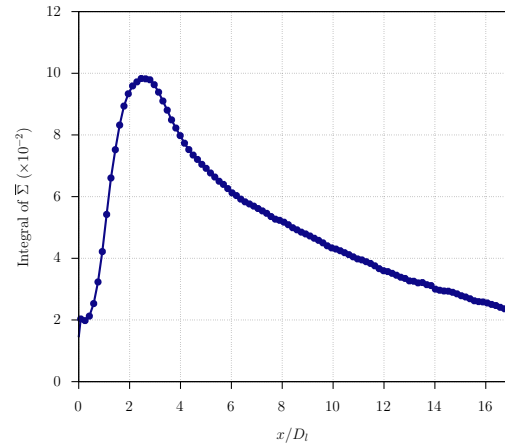


Figure 15: Integral along the x axis of the time-averaged surface density Σ

file, plotted on Figure 15, and the radial profiles, on Figure 16.

The shape of the axial profile of interfacial area density (fig. 15) shows that it rapidly grows downstream the injector to be the highest in the upstream zone of the spray (zone 2 fig. 6). Downstream, it slowly decreases as the flow goes far from the injector. Radial profiles of interfacial area density are plotted on Figure 16 at locations highlighted on Figure 6. Upstream, they show that a narrow region around the liquid jet concentrates the liquid-gas interface ($x = 0.5 D_t$). This can be easily explained by the low amplitude movement of the interface in this area that concentrates the Σ in the mean-field. Downstream, profiles become more and more wider as the gas-liquid mixing layer thickness increases. It is worth noting that profiles of Figures 15 and 16 provide a perfect data set to evaluate and validate future simulations that would use models to predict the evolution of Σ .

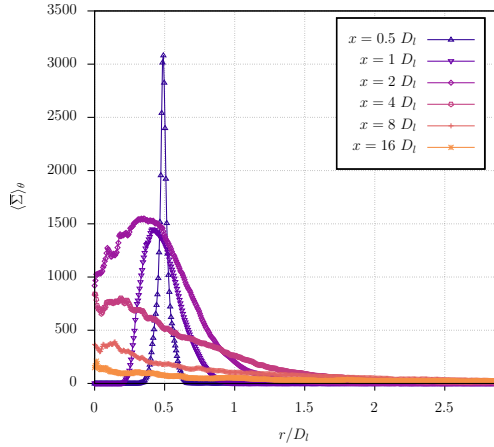


Figure 16: Radial profiles of spatial- and time-averaged surface density $(\bar{\Sigma})_{\theta}$.

In order to understand the consequences of atomization on the surface density it is interesting to correlate the map of the identified liquid structures and their classification with the surface density field. Figure 17 shows the averaged surface density near the injector plane along with the iso-contours obtained from the detection and classification of the detached structures presented in the previous section.

6.2. Mechanisms of surface density production

The mean field $\bar{\Sigma}$ is correlated with the map of the identified liquid structures and their classification on Figure 17, that shows the time-averaged interfacial area density in the upstream zone of the domain along with iso-contours obtained from the detection and classification of the detached structures presented in the previous sections. In this representation are displayed two types of iso-contours, the green represents the number of ligaments and the blue the number of spherical droplets detected as explained in section 5.4. For those two last quantities the same procedure of counting and azimuthal averaging has been performed as for Figure 11. The values have also been adimensionalized by the acquisition time of those quantities t_{acc} .

The atomization scenario proposed in the previous section is confirmed by Figure 17. The ligaments appear only after a destabilization distance of the injection plane. Indeed, the ligaments detach massively from the liquid core only around the abscissa $x/D_l = 1$. Spherical droplets resulting from ligament rupture appear further downstream in the flow than do ligaments. This observation confirms the scenario where atomization first passes over a ligament phase to generate droplets. Fi-

nally, the global shape of the spherical droplet contours in blue suggests a propagation of these structures due to the expansion of the spray.

Figure 17 illustrates the complexity of working with surface density. Indeed, the highest values of Σ visible are near the injection plane, where almost no structure exists. These high values are due to the slow movement of the interface which concentrates the instantaneous value of Σ . After this early stage, the jet expands and the Σ increases as the ligaments form. Then, the Σ seems to decrease as the spherical structures gradually replace the ligaments. This observation is very interesting because spontaneously one could think that the Σ will increase with the creation of a large number of small spherical droplets. However, an easy explanation for this decrease could be the minimisation of the surface when the liquid structures are in the form of spheres.

To visualise the evolution of Σ more precisely, Figure 18 a) shows the evolution of the integral of Σ along the x axis together with the integral of the number of ligaments and spherical droplets. The interfacial area density seems well correlated with the number of ligaments. Upstream, the location of maximal number of detached ligaments is the location of the peak of interfacial area density. Downstream, as ligaments are fast atomized and replaced by spherical droplets, the profile of Σ remains correlated with the destruction of ligaments and not to the creation of spherical droplets.

To go further into the understanding of interfacial area creation and destruction phenomena, Figure 18 b) (resp. c)) shows the evolution of the integral of the surface (resp. the volume) of the liquid core, detached ligaments and spherical droplets. The surface evolution shows that the liquid core concentrates most of the interfacial area upstream in the domain. The reason is that strong ripples and elongated structures are formed on the liquid core before they detach from it and are detected as detached ligaments and, under strong atomization, as spherical droplets. Downstream this zone, from $x = 6D_l$, volume of ligaments and spherical droplets remain similar but the surface of spherical droplets is twice or more greater than the surface of ligaments, while the interfacial area density continues to decrease. It means that when the surface tension forces increase compared to viscous forces, liquid structures become more spherical and that tends to decrease the interfacial area density.

These graphs also confirm once again the evolution of the liquid structures deduced from Figure 13. The structures break up like ligaments and then rapidly transform into numerous small spherical drops. First, the sur-

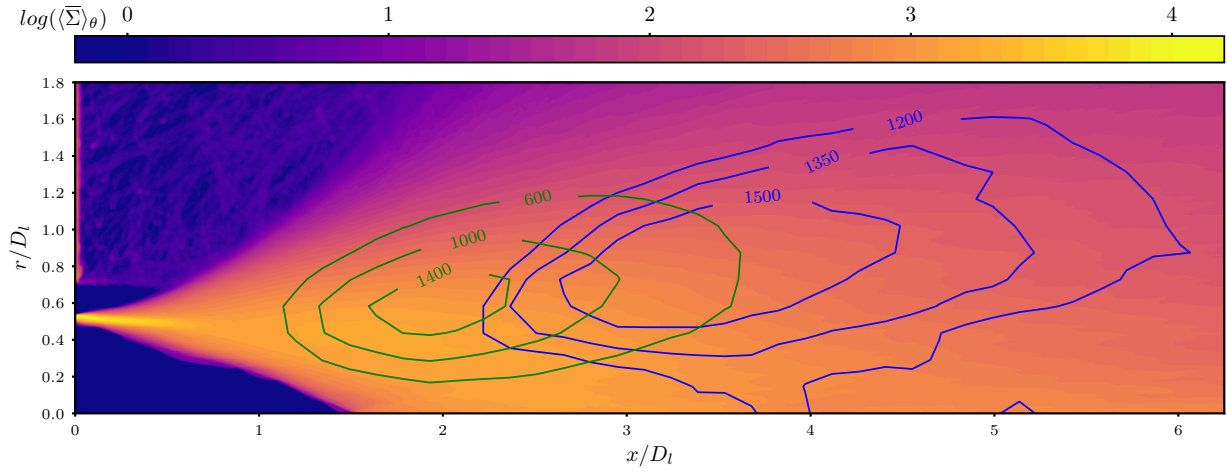


Figure 17: Half-cut of median plane colored by the spatial- and time-averaged surface density using a logarithmic scale, together with isolines of the number of ligament in green and isolines of the number of spherical structures in blue. The number of structures are adimensionalized by the acquisition time t_{acc} .

face created by the ligaments suddenly reaches a plateau around the abscissa $x/D_l = 2.5$. Secondly, this location corresponds to the peak of Σ and ligaments number, meaning the ligaments start to disappear in this location. Finally, the location also corresponds to a strong increase in the number of spherical droplets because the ligaments are massively transformed into droplets at this location.

Downstream the abscissa $x/D_l = 5$, the decrease of surface density is still induced by stabilising ligaments in spherical droplets, but another phenomenon seems to contribute to the decrease of Σ . As the flow progresses, fewer and fewer structures are present in the area while they become larger on average. The overall enlargement of the structures is visible in Figures 18 a) and c) as the overall volume increases while the number of structures decreases, especially for ligament structures. Indeed, in zone 3, atomization creates larger structures coming directly from the core with a low velocity aligned with the x -axis, so these structures remain in the field longer than tiny droplets. Dumouchel *et al.* described this phenomenon as structural atomization.

It is worth noting that a deeper analysis of interfacial area on the liquid core could allow to better understand the interfacial area density spatial evolution in the domain. Some methodologies, proposed for example by Dumouchel *et al.* [58], are very promising for studying the local topology of large structures like the liquid core.

6.3. Mechanisms of surface density reduction

In the previous section, the results in Figures 18 b) and c) showed a constant increase in the total volume of droplets with the distance from the injector. Conversely, the corresponding surface presented an initial increase up to a peak, and subsequently a decline. These results may suggest that the detached liquid structures tend to stabilise and become more spherical with the distance from the injection. This last section therefore focuses on the stabilization achieved by the liquid structures and on the characterisation of their average sizes at the end of the domain.

The evolution of total volume structures in Figure 18 c) shows a sort of plateau after $x/D_l = 7$, especially for the detached ligaments. At the same time Figure 18 b) shows a decrease in the global surface. These two remarks combined show that liquid structures tend to stabilise into more spherical structures. To highlight the stabilization and quantify the characteristic size of the liquid structures across the domain, Figure 12 shows the local size distribution of the structures. The same methodology of clustering and azimuthal average (as in Figure 11) is employed here to make the Figure 12. However, in this figure, the numbers of structures are not simply added together but their characteristic diameters are averaged in each cluster. Using a simple average of droplet diameters in each cluster is not a really relevant option because it introduces a strong bias towards structures smaller than the cluster size. This is because several tiny droplets can fit into one cluster at a time, whereas a single structure fits into a cluster smaller than

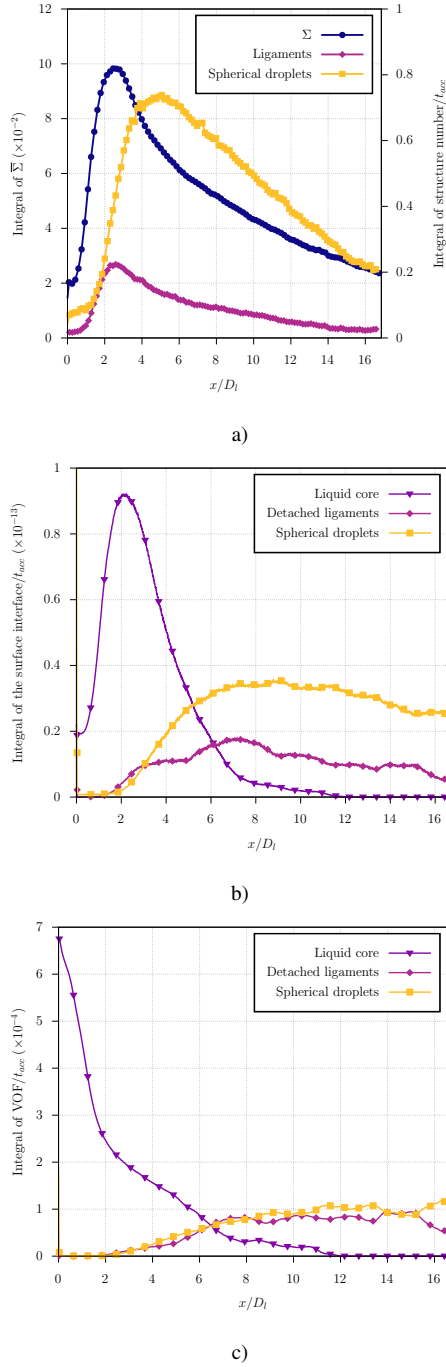


Figure 18: Integral along the x axis of a) the time-averaged surface density Σ , numbers of ligaments and spherical droplets, b) Surfaces of the liquid core, ligaments and spherical droplets, c) Volumes of the liquid core, ligaments and spherical droplets. Integral of number, surface and volume are adimensionalized by the acquisition time.

its own size.

cite eq d30

The D_v distribution has many features that can be discussed. First it confirms the conclusion made in the previous sections, the intense atomization in zone 2 generates very small droplets while the structures further downstream are much larger. Later on, the distribution shows a very high point around the abscissa $x/D_l = 5$ corresponding to large structures detaching from the intact core. As can be seen in the Figure 4, the location of this point corresponds rather well to the average length of the intact liquid core after the transient phase. In the following, the quantitative evolution of the characteristic diameter D_v will be evaluated with the help of profile extractions at certain locations, these are plotted in Figure 19. The locations of the extractions are indicated using the vertical dashed lines in Figure 12. A great deal of information can be deduced from these extractions, so lets go through these profiles from the closest to the injection to the furthest.

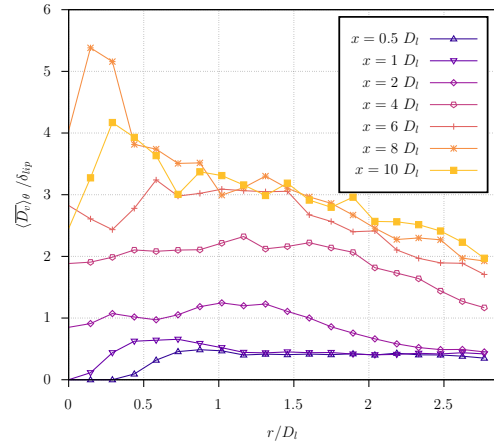


Figure 19: Radial profiles of characteristic diameter D_v .

First of all, the profiles at the locations $x/D_l = 0.5$ and $x/D_l = 1$ show no sign of atomization. Indeed, the only liquid droplets present after the core emphasis come from the recirculation zone. Only droplets with a characteristic size around $0.5 \delta_{lip}$ are small enough to be conducted by the recirculation flow. No droplets are directly created by the core in those locations, confirming the delay observed in the atomization process. Their average size below $0.5 \delta_{lip}$ is a direct consequence of the threshold of $2 dx = 0.34 \delta_{lip}$ chosen to consider a liquid structure in the statistical analysis. The profile located at $x/D_l = 2$ is way more interesting in term of atomization. Located upstream in zone 2, it shows clearly the consequence of atomization. The droplet created by

the atomization in this location shows a constant characteristic diameter D_v around $1.0 \delta_{lip}$. After the radius $r/D_l = 2$, the size of the liquid structures decreases and the profile matches the first two profiles. This indicates the end of the predominance of atomization coming directly from the core. The droplet size of about $0.5 \delta_{lip}$, clearly indicates that the recirculation zone is driving the structure size in this area. The following profile, located at $x/D_l = 4$, is the end of the strong atomization zone. This profile depicts two different phenomena. First, the average diameter increase in the spray passing from $1.0 \delta_{lip}$ in the profile $x/D_l = 2$ to $2.0 \delta_{lip}$ in this one. Secondly, as in the previous profile, the average size of the liquid structures decreases but this time much further away from the axis. Using the beginning of the decrease in size in the different profiles, it is possible to identify clearly the extent of the spray generated by the primary atomization. Finally, the domain is not large enough to completely reach the end of the spray emphasis in this profile. This explains why the droplet size does not collapse with the three previous profiles at large radial distances from the axis. The profile at $x/D_l = 8$ shows the largest structures with a strong peak near the axis. The peak corresponds to large structures released from the liquid core by textural atomization. After that, a trend similar to all previous profiles is visible with a decrease in size away from the axis. Finally, the last profile, located at $x/D_l = 10$, also shows a peak near the axis with a similar trend of decrease away from the axis. The particular observation here is the overall decrease in size compared to the $x/D_l = 8$ profile. This decrease in size could be explained by the global stabilization of the structures. Atomization would no longer play a determining role here and the structures would become more and more spherical decreasing their characteristic size.

To conclude and summarise all the observations made in this section, an attempt will now be made to highlight the overall trends. First of all, a clear correlation can be established between the position considered and the size of the structures. The average characteristic size of the structures is larger as you move away from the injection plane. Nevertheless, the overall size finally stops increasing in the area where atomization no longer plays a major role. The size of the structures even tends to slightly decrease at the end of the domain as the structures become more spherical. Secondly, after the profile $x/D_l = 2$ the trend in the structure size is to decrease going away from the axis. A clear difference can be observed in the profiles at $x/D_l = 2$ and $x/D_l = 4$ compared to the two last profiles located at $x/D_l = 8$ and $x/D_l = 16$. The first two are characterised by textural

atomization, in which very small droplets are created on the sides of the liquid core. The last two are characterised by structural atomization in which large structures, mainly small liquid core parts, are concentrated on the axis. However, the transition between these two regimes does not appear to be sharp. In textural atomization, the droplet size seems to be relatively constant and only correlated to the distance from the injection, the decrease in size only occurs at the exit of the spray influence. Whereas in structural atomization, large structures seem to be more concentrated near the axis with a continuous decrease in structure size away from the axis.

It is important to note here that the definition chosen for the characteristic size in equation (21) could play a major role in the conclusion made in this section, especially in absolute value given for specific sizes. Furthermore, as the velocity decreases rapidly with the distance from the injection, a large structure with a larger inertia can be taken into account several times in the same cluster, artificially increasing the local D_v value. However, this formulation was a better compromise than an unweighted formulation that would give excessive importance to small droplets, which would hide the very presence of large liquid structures in some locations. The best tool to assess the stabilization of structures in the flow would be the individual tracking of the structures. It would make it possible to specifically identify the liquid structures resulting from the atomization of attached ligaments but also to follow the evolution of the characteristics of liquid structures such as the Weber number.

7. Conclusion

This paper presents, to the best of the authors' knowledge, the most resolved simulation to date in a round coaxial injection configuration in fiber regime. A rapid gas flow is injected around a slow liquid flow. The fiber regime's high-velocity difference between gas and liquid creates an intense atomization process. After the global description, a specific effort was made to justify the numerical refinement of the calculation and the physical time considered. The analysis is organised following the flow progression. First, a frequency analysis was performed on the liquid core to investigate the origin of the atomization process. After that, the new detection algorithm named AlgoDetect is used to analyse the main atomization. The ligaments structures are put into perspective in the atomization process, and the relation with the evolution of the liquid-gas interface density were analysed. Finally, the focus was made on the

droplet's characteristic size in the spray and the stabilization of liquid structures in spheres. The analysis of the flow made it possible to specify the scenario occurring during atomization in the fiber regime. The use of AlgoDetect, the algorithmic detection of the droplet, made this whole study possible. It provides tremendous new and valuable data allowing the exploration of characteristic size or shape characterisation of the liquid structure. First of all the distribution of droplets resulting from the detection showed a zone near the injection where the liquid core is not perturbed enough to produce droplets. The atomization only starts after a delay, and nearly no droplets are formed in this area. The delay area is a zone where the ripples visible on the core since the injection start to grow. The analysis of the core ripples in this first zone brings to light a specific frequency amplified in the flow, which is undoubtedly the main origin of the whole atomization process of this regime. At some point in the liquid core, the interface ripples become large enough to create large pockets of liquid together with elongated structures attached to the core. After that, the atomization of those large structures creates a population of elongated detached ligaments. Very quickly, these detached ligaments are also atomised into numerous spherical droplets. The resulting droplets are finally too small to be significantly affected by the atomization.

The primary atomization just described is only observed in a fairly restricted area, not too close to the injection, to allow time for the disturbances to develop, but also not too far away, as the gas rapidly loses its kinetic energy by interacting with the liquid. The detached ligaments structures are a very good indicator of the progress of the atomization process. However, the analysis also showed that the major part of the surface causing the atomization is still attached to the core. Only a tiny part of the total liquid results in detached ligaments in a specific snapshot, mainly because the atomization of these structures is very fast. The liquid core is therefore an extremely complex structure to study, with one area quite smooth and another with many long attached structures. The complete analysis of the liquid core, which is not discussed in this article, is a very good avenue for future research on the subject. In addition to the primary atomization scenario just discussed, this article presents for the first time a detailed description of the liquid-gas interface density in assisted atomization configuration. Despite the difficulty of interpretation of this quantity, a relation between the structure evolution and this surface density is carefully made. It also describes the global growth of surface density that evolves counter-intuitively, with a strong peak of surface density

around the ligaments and a progressive decrease when the structures become spherical. The surface density profiles provided in this work will be essential for validating future LES simulations using the surface density as a model at the sub-grid scale. These data will be particularly relevant when considering the influence of elongated structures on the surface density model at the sub-grid scale. The last significant assessment of this work is about the evolution of the global droplet size. A strong correlation seems to link the location of the creation and the resulting characteristic size of structures. The droplets created at an early atomization stage are much smaller than those created later in the flow. In addition, due to their small inertia, the smaller droplets quickly follow the gas motion away from the axis. Those two observations induce a gradual replacement of the small structures and an increase of the average structure size in the domain.

The continuous growth of high performance computing allows the simulation described here, which can describe a flow as complex as coaxial atomization in fiber regime. Until recently, experimentation was the only way to gather data to validate the models used for the intermediate fidelity simulation. However, the experimentation has some limitations. In the zone where the liquid is still dense *i.e.* where atomization is taking place, only visual access is possible. Visual observations introduce a strong bias, firstly because of the superposition of structures in the field of view, and secondly because the measurement of structure size is only possible in the dispersed phase, far from the atomization site. This second type of measurement allows only an indirect validation of the resulting droplet size of the atomization. The DNS calculation presented in this article is a new and promising way to collect data for the validation of atomization models. For future studies, some improvements in post-processing should be made to help better understand the mechanism observed in atomization. The first point is tracking the evolution and displacement of individual structures. Structure tracking algorithms are already available in DYJEAT framework and could easily be applied in this type of simulation, but their cost is currently prohibitive in this configuration. Furthermore, the resulting relation tree analysis between the structures is not trivial. This type of analysis could allow a better understanding of the correlation between the place of creation and the size of the drops. Secondly, the article demonstrates that many valuable pieces of information are hidden from the current methodology because it does not study the fine structure of the entire liquid core. More advanced analysis of this central structure could provide a large amount of helpful infor-

mation.

References

- [1] A. H. Lefebvre and V. G. McDonell. *Atomization And Sprays*. CRC Press, 2017.
- [2] F. Ben Rayana. *Contribution à l'étude des instabilités interfaciales liquide-gaz en atomisation assistée et taille de gouttes*. PhD thesis, Grenoble INPG 2007, 2007.
- [3] A. Lozano, E. Calvo, J. A. García, and F. Barreras. Mode transitions in an oscillating liquid sheet. *Phys. Fluids*, 23:044103, 2011.
- [4] A. Mansour and N. Chigier. Dynamic behavior of liquid sheets. *Phys. Fluids A*, 3:2971–2980, 1991.
- [5] P. Marmottant and E. Villermaux. On spray formation. *J. Fluid Mech.*, 498:73–111, 2004.
- [6] M. Hong. *Atomisation et mélange dans les jets coaxiaux liquide-gaz*. PhD thesis, INPG, 2003.
- [7] J.-P. Matas and A. H. Cartellier. Flapping instability of a liquid jet. In *7th International Conference on Multiphase Flow ICMF 2010*, page 413, 2010.
- [8] A. Kumar and S. Sahu. Liquid jet breakup unsteadiness in a coaxial air-blast atomizer. *International Journal of Spray and Combustion Dynamics*, 10:211–230, 2018.
- [9] C. Larricq-Fourcade. *Étude de la pulvérisation assistée en air d'une nappe liquide et influence d'un vent ionique sur les instabilités hydrodynamiques*. Theses, ISAE, Université de Toulouse, 2006.
- [10] B. Dejean. *Experimental study of liquid sheet atomization with and without prefilming zone for its modelling - Boundary condition influence*. PhD thesis, Institut Supérieur de l'Aéronautique et de l'Espace (ISAE), 2015.
- [11] V. Gutiérrez Fernández. *Experimental study of liquid sheet disintegration in a high pressure environment*. Theses de doctorat, Institut Supérieur de l'Aéronautique et de l'Espace (ISAE), 2009.
- [12] Z. Farago and N. Chigier. Morphological classification of disintegration of round liquid jets in a coaxial air stream. *Atomization Sprays*, 1992.
- [13] J.-C. Lasheras and E.-J. Hopfinger. Liquid jet instability and atomization in a coaxial gas stream. *Annu. Rev. Fluid Mech.*, 32:275–308, 2000.
- [14] Y. Liang, L. C. Johansen, and M. Linne. Breakup of a laminar liquid jet by coaxial non-swirling and swirling air streams. *Phys. Fluids*, 34:093606, 2022.
- [15] O. Desjardins, J. McCaslin, M. Owkes, and P. Brady. Direct numerical and large-eddy simulation of primary atomization in complex geometries. *Atomization Sprays*, 23:1001–1048, 2013.
- [16] M. Herrmann. A parallel eulerian interface tracking/lagrangian point particle multi-scale coupling procedure. *J. Comput. Phys.*, 229:745–759, 2010.
- [17] G. Tomar, D. Fuster, S. Zaleski, and S. Popinet. Multiscale simulations of primary atomization. *Comput. Fluids*, 39:1864–1874, 2010.
- [18] Y. Ling, S. Zaleski, and R. Scardovelli. Multiscale simulation of atomization with small droplets represented by a lagrangian point-particle model. *Int. J. Multiphase Flow*, 76:122–143, 2015.
- [19] M. Sussman and E. G. Puckett. A coupled level set and volume-of-fluid method for computing 3d and axisymmetric incompressible two-phase flows. *J. Comput. Phys.*, 162:301–337, 2000.
- [20] T. Ménard, S. Tanguy, and A. Berlemont. Coupling level set/vof/ghost fluid methods: Validation and application to 3d simulation of the primary break-up of a liquid jet. *Int. J. Multiphase Flow*, 33:510–524, 2007.
- [21] J. Shinjo and A. Umemura. Surface instability and primary atomization characteristics of straight liquid jet sprays. *Int. J. Multiphase Flow*, 37:1294–1304, 2011.
- [22] X. Li and M. C. Soteriou. Detailed numerical simulation of liquid jet atomization in crossflow of increasing density. *Int. J. Multiphase Flow*, 104:214–232, 2018.
- [23] N. Odier, G. Balarac, C. Corre, and V. Moureau. Numerical study of a flapping liquid sheet sheared by a high-speed stream. *Int. J. Multiphase Flow*, 77:196–208, 2015.
- [24] D. Zuzio, J.-L. Estivalèzes, and B. DiPierro. An improved multi-scale eulerian-lagrangian method for simulation of atomization process. *Computers and Fluids*, 176:285–301, 2018.
- [25] G. Agbaglah, R. Chiodi, and O. Desjardins. Numerical simulation of the initial destabilization of an air-blasted liquid layer. *J. Fluid Mech.*, 812:1024–1038, 2017.
- [26] Y. Ling, D. Fuster, G. Tryggvason, and S. Zaleski. A two-phase mixing layer between parallel gas and liquid streams: multi-phase turbulence statistics and influence of interfacial instability. *J. Fluid Mech.*, 859:268–307, 2019.
- [27] D. Jiang and Y. Ling. Destabilization of a planar liquid stream by a co-flowing turbulent gas stream. *Int. J. Multiphase Flow*, 122:103121, 2020.
- [28] F. Xiao, M. Dianat, and J.J. McQuirk. Les of turbulent liquid jet primary breakup in turbulent coaxial air flow. *Int. J. Multiphase Flow*, 60:103–118, 2014.
- [29] G. Charalampous, Y. Hardalupas, and A. Taylor. Structure of the continuous liquid jet core during coaxial air-blast atomisation. *International Journal of Spray and Combustion Dynamics*, 1:389–415, 2009.
- [30] T. Müller, A. Sängler, P. Habisreuther, T. Jakobs, D. Trimis, T. Kolb, and N. Zarzalis. Simulation of the primary breakup of a high-viscosity liquid jet by a coaxial annular gas flow. *Int. J. Multiphase Flow*, 87:212–228, 2016.
- [31] F. Zhang, T. Zirwes, T. Müller, S. Wächter, T. Jakobs, P. Habisreuther, N. Zarzalis, D. Trimis, and T. Kolb. Effect of elevated pressure on air-assisted primary atomization of coaxial liquid jets: Basic research for entrained flow gasification. *Renewable Sustainable Energy Rev.*, 134:110411, 2020.
- [32] G. Blanchard, P. Villedieu, and D. Zuzio. Numerical simulation of primary atomization of a sheared liquid sheet. part 1: model and numerical method description. In *ILASS Europe*, 2013.
- [33] G. Blanchard, P. Villedieu, and D. Zuzio. Numerical simulation of primary atomization of a sheared liquid sheet. part 2: comparison with experimental results. In *ILASS Europe*, 2013.
- [34] P. Gaillard, C. Le Touze, L. Matuszewski, and A. Murrone. Numerical Simulation of Cryogenic Injection in Rocket Engine Combustion Chambers. *Aerospace Lab*, page 16, 2016.
- [35] C. Le Touze, L.H. Dorey, N. Rutard, and A. Murrone. A compressible two-phase flow framework for Large Eddy Simulations of liquid-propellant rocket engines. *Appl. Math. Model.*, 84:265–286, 2020.
- [36] A. Vallet. *Contribution à la modélisation de l'atomisation d'un jet liquide haute pression*. PhD thesis, Université de Rouen Normandie, 1997.
- [37] A. Vallet and R. Borghi. Modélisation eulerienne de l'atomisation d'un jet liquide. *Comptes Rendus de l'Académie des Sciences - Series IIB - Mechanics-Physics-Astronomy*, 327:1015–1020, 1999.
- [38] S. Jay, F. Lacas, and S. Candel. Combined surface density concepts for dense spray combustion. *Combust. Flame*, 144:558–577, 2006.

- [39] R. Lebas, T. Menard, P.A. Beau, A. Berlemont, and F.X. Demoulin. Numerical simulation of primary break-up and atomization: DNS and modelling study. *Int. J. Multiphase Flow*, 35:247–260, 2009.
- [40] B. Duret. Simulation numérique directe des écoulements liquide-gaz avec évaporation : application à l’atomisation. PhD thesis, INSA Rouen, 2013.
- [41] J. Chesnel, J. Reveillon, T. Menard, and F.-X. Demoulin. Large eddy simulation of liquid jet atomization. *Atomization Sprays*, 21:711–736, 2011.
- [42] J. Anez, A. Ahmed, N. Hecht, B. Duret, J. Reveillon, and F.X. Demoulin. Eulerian–lagrangian spray atomization model coupled with interface capturing method for diesel injectors. *Int. J. Multiphase Flow*, 113:325–342, 2019.
- [43] L. Palanti, S. Puggelli, L. Langone, A. Andreini, J. Reveillon, B. Duret, and F.X. Demoulin. An attempt to predict spray characteristics at early stage of the atomization process by using surface density and curvature distribution. *Int. J. Multiphase Flow*, 147:103879, 2022.
- [44] F. Couderc. Development of a numerical code for the simulation of non-miscible fluid flow. Application to the air-assisted disintegration of a liquid jet. PhD thesis, Ecole nationale supérieure de l’aéronautique et de l’espace, 2007.
- [45] T. Xavier, D. Zuzio, M. Averseng, and J.-L. Estivalèzes. Toward direct numerical simulation of high speed droplet impact. *Meccanica*, pages 1–15, 2019.
- [46] M. Averseng, D. Zuzio, A. Boutsikakis, and J.-L. Estivalèzes. DNS simulation and analysis of periodic planar liquid sheet assisted atomization. In *10th International Conference on Multiphase Flow (ICMF 2019)*, 2019.
- [47] D. Zuzio, A. Orazzo, J.-L. Estivalèzes, and I. Lagrange. A new efficient momentum preserving level-set/VOF method for high density and momentum ratio incompressible two-phase flows. *J. Comput. Phys.*, 410:109342, 2020.
- [48] M. Sussman, P. Smereka, and S. Osher. A level set approach for computing solutions to incompressible two-phase flow. *J. Comput. Phys.*, 114:146–159, 1994.
- [49] D. L. Youngs. Time-dependent multi-material flow with large fluid distortion. *Numerical Methods for Fluid Dynamics*, 1982.
- [50] J. López and J. Hernández. Analytical and geometrical tools for 3d volume of fluid methods in general grids. *J. Comput. Phys.*, 227:5939–5948, 2008.
- [51] R. P. Fedkiw, T. Aslam, B. Merriman, and S. Osher. A non-oscillatory eulerian approach to interfaces in multimaterial flows (the ghost fluid method). *J. Comput. Phys.*, 152:457–492, 1999.
- [52] M. Averseng. Contribution à la modélisation de l’atomisation assistée par l’analyse de simulations haute fidélité. PhD thesis, ISAE Toulouse, 2022.
- [53] N. Rutard, L.-H. Dorey, C. Le Touze, and S. Ducruix. Large-eddy simulation of an air-assisted liquid jet under a high-frequency transverse acoustic forcing. *Int. J. Multiphase Flow*, 122:103144, 2020.
- [54] A. Ficuciello, J.B. Blaisot, C. Richard, and F. Baillot. Investigation of air-assisted sprays submitted to high frequency transverse acoustic fields: Droplet clustering. *Phys. Fluids*, 29:067103, 2017.
- [55] A. Ficuciello. Analysis of high frequency/high amplitude acoustic field effects on coaxial injection : application to liquid rocket engines. PhD thesis, Université de Rouen, 2018.
- [56] I. Lagrange, A. Orazzo, D. Zuzio, and J.-L. Estivalèzes. Immersed interface method for the direct numerical simulation of air-blast primary atomization. In *ILASS America*, 2017.
- [57] N. Rutard. Simulation numérique et modélisation de l’influence d’ondes acoustiques de haute amplitude sur un jet diphasique : application au domaine de la propulsion fusée à ergols liquides. PhD thesis, Université Paris-Saclay, 2020.
- [58] C. Dumouchel, J.-B. Blaisot, F. Abuzahra, A. Sou, G. Godard, and S. Idlahcen. Analysis of a textural atomization process. *Exp. Fluids*, 60, 2019.